Design of a Swept-Source, Anatomical OCT System for Pediatric Bronchoscopy

Kushal C. Wijesundara[a], Nicusor V. Iftimia[c], and Amy L. Oldenburg[a,b]
[a]Department of Physics and Astronomy and the [b]Biomedical Research Imaging Center, University of North Carolina at Chapel Hill, Chapel Hill, NC 27599-3255
[c]Physical Sciences Inc., New England Business Center, Andover, MA 01810

ABSTRACT

We describe the design and performance of a long coherence length, swept-source anatomical OCT (aOCT) system for pediatric airway imaging. A fiber-optic catheter is designed to be accommodated by a small-bore bronchoscope, and is scanned distally in a helical scan pattern to provide aOCT during bronchoscopy. We discuss particular challenges associated with the need for large imaging range, low SNR roll-off, and small catheter diameter. We present 3-D visualizations of airway phantoms and discuss optimization of the airway surface geometry obtained by aOCT. Accurate reconstruction of airway geometry will enable predictive modeling of patients suffering from airway obstruction.

Keywords: Anatomical Optical Coherence Tomography, Pediatric Airway Imaging, Mach-Zehnder Fiber-Optic Interferometer, Signal to Noise Ratio, Digital Dispersion Compensation, 3D Image Rendering

1. INTRODUCTION

Children with upper airway abnormalities often exhibit multiple levels of airway obstruction that lead to insufficient respiration and morbidity. Quantitative methods of evaluating pediatric airways would enhance clinical decision-making. Anatomical OCT (aOCT) addresses this need by providing an extended depth scan range to assess large-scale structures such as the upper airway [1,2]. In particular, the accurate reconstruction of surface geometry enables computational models to study airflow characteristics [3] which may be useful for predicting patient outcomes after surgery.

Here we describe the design of a swept-source, aOCT system for imaging the geometry of pediatric airways during bronchoscopy. While most previous aOCT studies have employed time-domain OCT systems, the use of long coherence length swept-source OCT systems are beginning to be explored for applications in ophthalmology [4] and imaging vocal folds [5]. The need for pediatric bronchoscopy presents the particular challenge of providing sufficiently long imaging radius (>12 mm) in combination with a sufficiently small diameter catheter (<1.2 mm) to fit the bore of the smallest commercial bronchoscope used in infants. To our knowledge, this combination of features has not yet been reported. In contrast to methods where aOCT is performed through a nasal tube, bronchoscopic-capable OCT permits imaging of lower airways [6], and enables concomitant video imaging with which clinicians are already comfortable.

2. INSTRUMENT DESIGN

The aOCT system consists of a 20 mW wavelength-swept light source (Santec, Inc) centered at 1305 nm with a sweep rate of 5 kHz, a sweep range of 30 nm (corresponding to an axial resolution of 25 μm), and, importantly, a coherence length of ~17.5 mm (1/*e* length) as measured experimentally. The light from the source is directed into a Mach-Zehnder fiber interferometer to perform aOCT. A 1×2 5/95 coupler divides the beam into the reference and sample arms, respectively. The reference arm consists of a collimator and adjustable delay retro-reflector. Circulators were used in both sample and reference arms to redirect the back-reflected light to a 2×2 50/50 fiber coupler, and the resulting interference was detected by a balanced

Optical Coherence Tomography and Coherence Domain Optical Methods in Biomedicine XVII, edited by James G. Fujimoto, Joseph A. Izatt, Valery V. Tuchin, Proc. of SPIE Vol. 8571, 85713K
 · doi: 10.1117/12.2004226

photodetector digitized at 10 MHz. Software was written in LabVIEW to simultaneously control the translational and rotational motion of the scan engine while digitizing the OCT signal. The schematic representation of the aOCT system is illustrated in Figure 1.

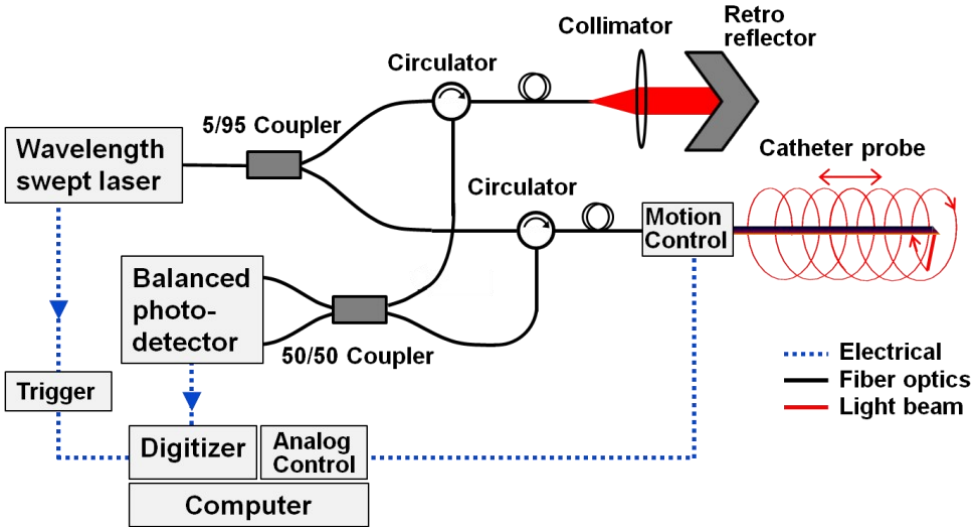

Figure 1. Schematic diagram of the anatomical optical coherence tomography (aOCT) system. Here the collimator and retro-reflector arm acts as the reference while the sample arm consists of the catheter probe.

A scanning engine (Physical Sciences, Inc) containing a fiber rotary junction and a custom fiber catheter are used in the sample arm of the interferometer to generate a helical scan pattern on the sample surface. The scanning engine provides a translational motion at up to 10 mm/s and full 360° rotational scans at up to 35 rotations/s. The fiber-optic catheter has a specially designed distal end consisting of fused glass spacer and a ball lens polished at 45 deg which provides a sideways-directed beam of focal length 3.5 mm and a long working distance, as demonstrated below. The ability to produce a long focal length is diffraction-limited by the aperture size at the catheter tip, which dictates a tradeoff between small catheter diameter and long focal length. In this first-stage design, we found that a sufficiently long working distance (>12 mm) is provided by a catheter of 0.64 mm outer diameter (OD) protected by a Fluorinated ethylene propylene or FEP tube (0.84 mm OD), which is sufficiently small for insertion into a small-bore pediatric bronchoscope.

3. RESULTS AND DISCUSSION

3.1 System Performance

The increased depth range afforded by aOCT provides the capability to image the air-tissue interface inside the human airway. Therefore, it is of primary importance to understand the relative contributions to OCT signal degradation as a function of depth, which can inform further aOCT system optimization. Here we experimentally compare the effects of focusing, coherence length, and *k*-space nonlinearity.

In the usual way, we define the signal-to-noise ratio (SNR) as that obtained from an aligned mirror at depth z. The peak aOCT signal amplitude $S(z)$ was measured for z = 2.5-14.5 mm. We attenuated the sample beam to prevent saturation of the photodetector, and recorded the power back-reflected from the mirror with no attenuation as $P_0(z)$, and the arbitrarily attenuated power as $P(z)$. Finally, the noise, $N(z)$, was computed as the standard deviation at depth z from an image with no sample but when the sample beam was at full power

(unattenuated); importantly, this accounts for any additional shot noise that would not be present in the attenuated image. Thus, we infer the true (operational) SNR in the absence of attenuation according to:

$$SNR(z) = 20\log_{10}\left(\sqrt{\frac{P_0(z)}{P(z)}}\frac{S(z)}{N(z)}\right) \quad (1)$$

The results of our measurements are summarized in Figure 2, and indicate a total rolloff of 21 dB at a depth of z = 14.5 mm.

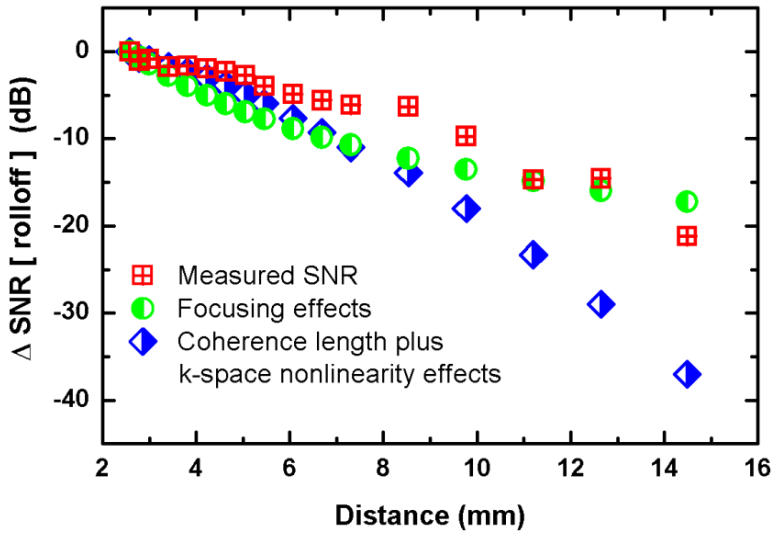

Figure 2. Variation of SNR with distance from the catheter tip (SNR rolloff). Here we plot the rolloff of the total measured SNR, the predicted rolloff of SNR due to the swept-source coherence length plus *k*-space nonlinearity, and the predicted rolloff due to catheter tip focusing effects.

To understand the relative contributions to this rolloff, we first realize that the effect of focusing is to reduce the reflected power, $P_0(z)$, and thus we have plotted the contribution of finite focusing as $10\log_{10}(P_0(z)/P_0(z = z_{focus}))$. We find that focusing appears to cause ~17.2 dB rolloff at z = 14.5 mm. Next, we investigated the effects of rolloff due to finite coherence length plus *k*-space nonlinearity by fixing the mirror near the focus and scanning the reference arm delay length (providing a relative delay, z), while measuring SNR from the aOCT image as before (where now $P(z)$ is effectively constant). In this method, we find that the rolloff is quite severe, at 37 dB at 14.5 mm. To isolate the coherence length from the *k*-space nonlinearity, we measured reference position corresponding to the 1/*e* decay point of the peak-to-peak voltage amplitude of the interference waveform, resulting in a coherence length of 17.5 mm and thus a predicted rolloff from coherence length only of 7.2 dB at 14.5 mm. This suggests that the coherence length of our light source plays only a small role in the total rolloff observed in our system, and that our reference scanning method predicts a much greater rolloff than we actually observe when samples are placed at great depths. This ambiguity may be due to depth-dependent noise, and suggests the need for a better noise model.

3.2 Digital Dispersion Compensation

Dispersion effects arise due to differences in the relative amount of fiber and free space in the reference and sample arms, the *k*-space nonlinearity, and dispersion in the sample itself. Digital methods of dispersion compensation are flexible in that they can provide both arbitrary fixed and depth-dependent dispersion

correction. There have been many techniques utilized to digitally compensate for dispersion effects as discussed in the literature [7-9]. Our approach consists of an autofocus algorithm based on an entropy minimization method originally developed for time-domain OCT [10], but now extended to swept-source OCT. With this method the *k*-space nonlinearity and interferometer imbalance effects are removed to obtain further improvement in our operational rolloff, as illustrated in the main plot of Figure 3.

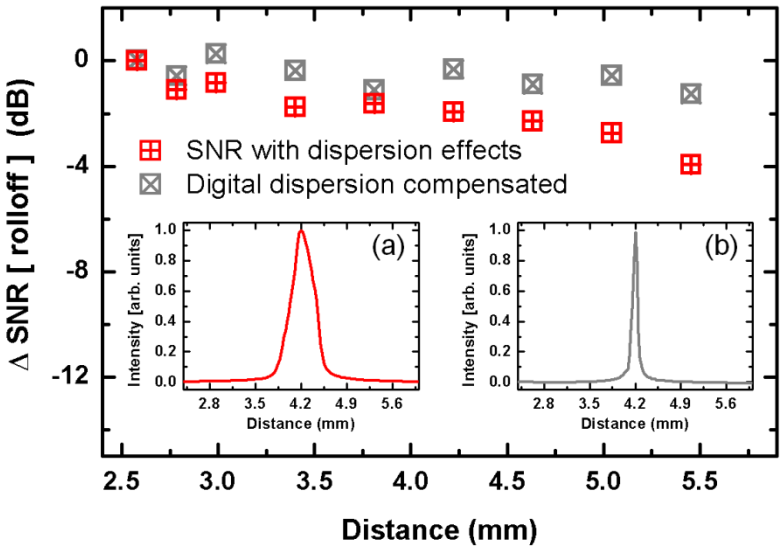

Figure 3. The main plot illustrates the variation of SNR with and without digital dispersion compensation. Inset: M-mode average A-line from OCT images of a mirror at 4.2 mm, (a) without dispersion compensation (b) with dispersion compensation.

Furthermore, in the current dispersion compensation technique, we fit the first, second, and third-order parameters for both fixed and depth-dependent dispersion (α and β in Ref. [10]) based on M-mode images of a mirror at different depths. The calibrated dispersion-corrected parameters were then incorporated into a custom Matlab script which is used for automated dispersion correction of subsequent aOCT images. As shown in Figure 3, much superior and sharper images can be obtained in this way. This dispersion method is capable, in future work, of being integrated into a real-time algorithm for image display.

3.3 3D Image Reconstruction

To verify the imaging depth of our system, we scanned a diffusely scattering piece of paper and found contrast to the paper surface up to ~12 mm (Figure 4); this maximum distance in practice will depend upon the scattering coefficient of airways and the obliqueness of the airway surface to the imaging beam.

Next, we performed a helical scan of a 13 mm inner diameter plastic tube with a linear scan speed of 5 mm/s and a rotational rate of 15 Hz. A custom Matlab script was employed to resample the data into a Cartesian space, and the software package ImageSurfer (UNC Chapel Hill) was employed to render the tube isosurface in 3D (Figure 4). While some variation of the rendered surface from a perfect cylinder is observed, we expect this noise to be suppressed when the catheter tip is confined within the bronchoscope bore. Current efforts to quantify this spatial variation from the true object surface will serve to guide optimization of the catheter mechanics.

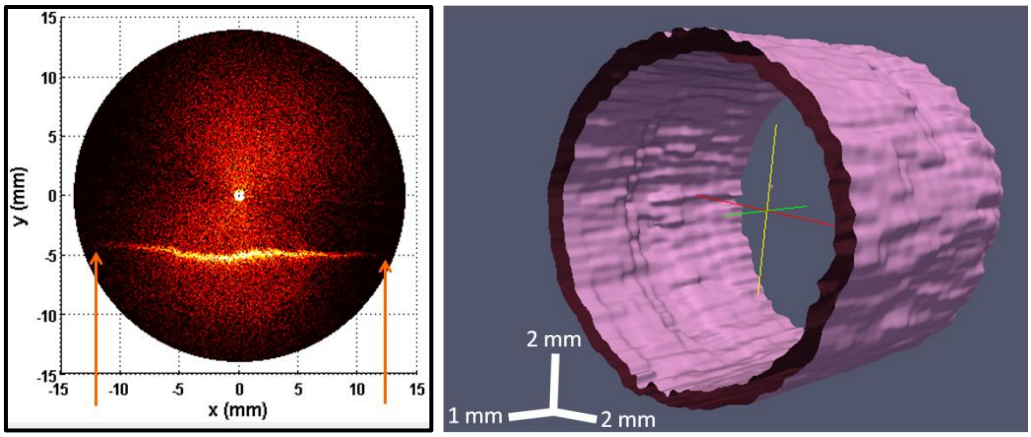

Figure 4. (Left): 2-D aOCT image of paper demonstrating contrast up to an imaging radius of 12 mm, as indicated by arrows. (Right): 3-D reconstruction of a 13 mm diameter plastic tube from a helical data scan.

4. CONCLUSION

In summary, we demonstrate an aOCT system capable of being deployed with a small diameter bronchoscope used in infants, while maintaining a sufficiently large imaging range for assessing airways up to 24 mm diameter. Quantitative methods for assessing the SNR rolloff and the rendered surface geometry are crucial for optimization of this device for clinical imaging of children with obstructive airways, which will enable accurate predictions of air flow and respiratory function.

5. ACKNOWLEDGEMENTS

This work was supported in part by the National Heart, Lung, and Blood Institute at the National Institutes of Health under grants R21HL111968 (Oldenburg), R21HL109832 (Oldenburg), R01HL105241 (Davis), and R01HL092964 (Boucher). The authors would like to thank members of the Pediatric Airways Group at the University of North Carolina at Chapel Hill for their helpful discussions.

REFERENCES

[1] Armstrong, J., Leigh, M., Walton, I., Zvyagin, A., Alexandrov, S., Schwer, S., Sampson, D., Hillman, D. and Eastwood, P., "In vivo size and shape measurement of the human upper airway using endoscopic long-range optical coherence tomography," Optics Express, 11(15), 1817-1826 (2003).

[2] Armstrong, J. J., Leigh, M. S., Sampson, D. D., Walsh, J. H., Hillman, D. R. and Eastwood, P. R., "Quantitative upper airway imaging with anatomical optical coherence tomography," Am. J. Respir. Crit. Care Med. 173(2), 226 (2006).

[3] Lucey, A. D., King, A. J., Tetlow, G. A., Wang, J., Armstrong, J. J., Leigh, M. S., Paduch, A., Walsh, J. H., Sampson, D. D., Eastwood, P. R., Hillman, D. R., "Measurement, reconstruction and flow-field computation of the human pharynx with application to sleep apnea," IEEE Trans. Biomed. Eng., 57(10), 2535-2548 (2010).

[4] Potsaid, B., Baumann, B., Huang, D., Barry, S., Cable, A. E., Schuman, J. S., Duker, J. S. and Fujimoto J. G., "Ultrahigh speed 1050nm swept source / Fourier domain OCT retinal and anterior segment imaging at 100,000 to 400,000 axial scans per second," Optics Express, 18(19), 20029-20048 (2010).

[5] Liu, G., Rubinstein, M., Saidi, A., Qi, W., Foulad, A., Wong, B. and Chen Z., "Imaging vibrating vocal folds with a high speed 1050 nm swept source OCT and ODT," Optics Express, 19(12) 11880-11889 (2011).

[6] Su, J., Zhang, J., Yu, L., Colt, G. H., Brenner, M. and Chen, Z., "Real-time swept source optical coherence tomography imaging of the human airway using a microelectromechanical system endoscope and digital signal processor," J. Biomed. Optics, 13(3), 030506-1 (2008).

[7] Kohlhaas, A., Fromchen, C. and Brinkmeyer E., "High resolution OCDR for testing integrated-optical waveguides: dispersion-corrupted experimental data corrected by a numerical algorithm," J. Lightwave Technol. 9(11), 1493-1502 (1991).

[8] Fercher, A., Hitzenberger, C., Sticker, M., Zawadzki, R., Karamata, B. and Lasser, T., "Numerical dispersion compensation for partial coherence interferometry and optical coherence tomography," Optics Express 9(12), 610-615 (2001).

[9] Yung, K. M., Lee, S. L. and Schmitt, J. M., "Phase-domain processing of optical coherence tomography images," J. Biomed. Opt. 4(1), 125-136 (1999).

[10] Marks, D. L., Oldenburg, A. L., Reynolds, J. J. and Boppart, S. A., "Autofocus algorithm for dispersion correction in optical coherence tomography," Appl. Optics, 42(16), 3038-3046 (2003).